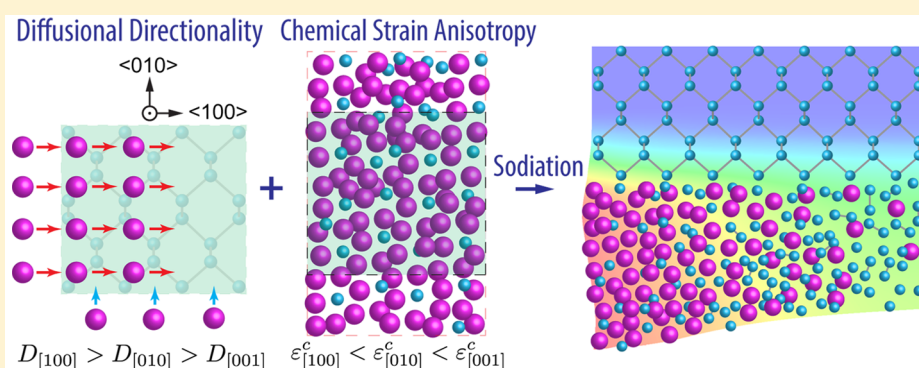# Two-Fold Anisotropy Governs Morphological Evolution and Stress Generation in Sodiated Black Phosphorus for Sodium Ion Batteries

Tianwu Chen,[†] Peng Zhao,[†] Xu Guo,[‡] and Sulin Zhang*[,†]

[†]Department of Engineering Science and Mechanics, and Materials Research Institute, The Pennsylvania State University, University Park, Pennsylvania 16802, United States

[‡]State Key Laboratory of Structural Analysis for Industrial Equipment, Department of Engineering Mechanics, International Research Center for Computational Mechanics, Dalian University of Technology, Dalian 116023, People's Republic of China

S Supporting Information

ABSTRACT: Phosphorus represents a promising anode material for sodium ion batteries owing to its extremely high theoretical capacity. Recent in situ transmission electron microscopy studies evidenced anisotropic swelling in sodiated black phosphorus, which may find an origin from the two intrinsic anisotropic properties inherent to the layered structure of black phosphorus: sodium diffusional directionality and insertion strain anisotropy. To understand the morphological evolution and stress generation in sodiated black phosphorus, we develop a chemo-mechanical model by incorporating the intrinsic anisotropic properties into the large elasto-plastic deformation. Our modeling results reveal that the apparent morphological evolution in sodiated black phosphorus is critically controlled by the coupled effect of the two intrinsic anisotropic properties. In particular, sodium diffusional directionality generates sharp interphases along the [010] and [001] directions, which constrain anisotropic development of the insertion strain. The coupled effect renders distinctive stress-generation and fracture mechanisms when sodiation starts from different crystal facets. In addition to providing a powerful modeling framework for sodiation and lithiation of layered structures, our findings shed significant light on the sodiation-induced chemo-mechanical degradation of black phosphorus as a promising anode for the next-generation sodium ion batteries.

KEYWORDS: Sodium ion batteries, black phosphorus, anisotropic swelling, chemo-mechanical modeling, stress generation

Cost-effective sodium (Na) ion batteries (NIBs) have recently drawn significant interests for their potential applications in future renewables-friendly, grid-scale energy storage.[1,2] Though the similar chemistry enables accessible design strategies for NIBs parallel to lithium ion battery (LIB) technologies,[3,4] it has remained a challenge to identify high-performance electrode materials compatible for sodium ions. Graphite, the most popular anode used in commercial LIBs, cannot be directly used as anode for NIBs because of the larger size of Na ions than Li ions and correspondingly the higher intercalation barrier.[5,6] Silicon (Si), one of the most promising next-generation anode materials for LIBs, is inert to sodium insertion at room temperature.[7] Phosphorus (P) and phosphorus-based compounds represent a promising new class of anode materials for NIBs[8,9] for their much higher theoretical capacity (Na_3P, ~2600 mAh/g) than both carbon-

based materials (e.g., hard carbon, ~300 mAh/g) and intermetallic alloys (e.g., Sn and Sb, ~600−900 mAh/g).[10−12] However, similar to intermetallic alloy anodes (e.g., Si and Ge) for LIBs, phosphorus undergoes huge volume change (~400%) during sodiation/desodiation,[13] leading to pulverization of the active materials, unstable growth of solid-electrolyte interphase (SEI), and fast capacity fading.[14,15] In terms of its high capacity and large volume change, phosphorus in NIBs can be regarded as the counterpart of Si in LIBs. Despite rapid progress in understanding the lithiation-induced failure[16−30] and novel designs of Si anodes for LIBs,[31−37] the degradation mechanism
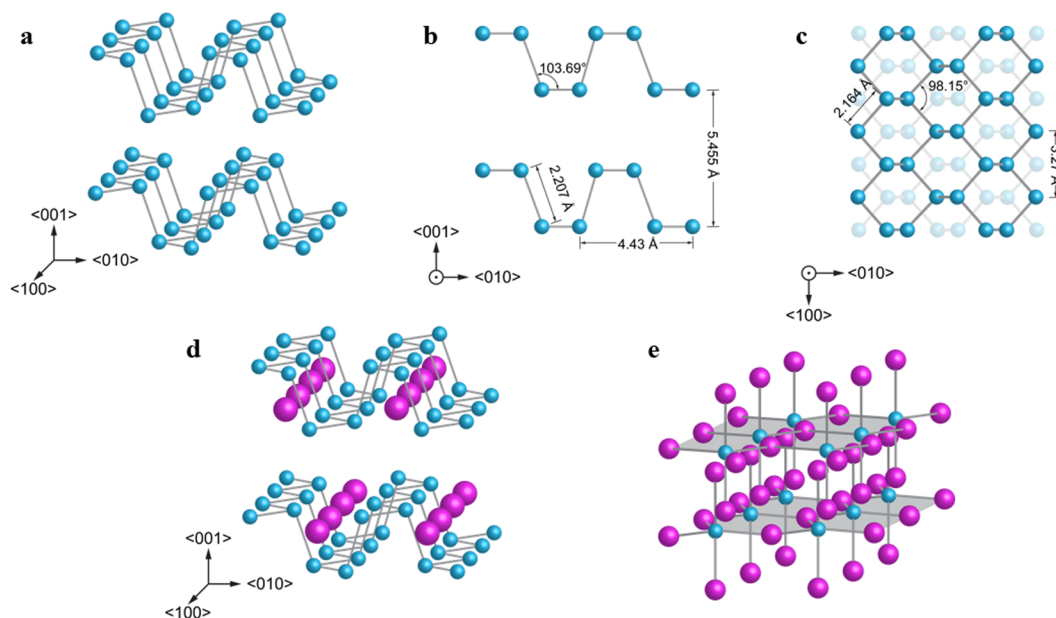
Figure 1. Crystal structure of black phosphorus and its sodiation mechanism. (a–c) The 3D, front, and top view of black phosphorus, respectively. (d) In the first step of sodiation, sodium ions are intercalated into the interlayer space to form $Na_{0.25}P$. (e) In the second step of sodiation, the phosphorus is alloyed to form Na_3P. Blue particles, phosphorus; purple particles, sodium.

of phosphorus during sodiation/desodiation cycles has remained largely unexplored.

Herein, we formulate a chemo-mechanical model to simulate morphological evolution and stress generation in black phosphorus during sodiation. The model couples sodium diffusion and anisotropic insertion strain with large elastic-plastic deformation in the three-dimensional (3D) setting. Our simulation results reveal that two intrinsic anisotropies, sodium diffusional directionality and insertion strain anisotropy, influence one another, and together they control the morphological evolution and stress generation in sodiated black phosphorus. Our mechanistic understanding provides guidance to mitigate degradation of the high-capacity anodes for NIBs.

Among the three main allotropes of phosphorus (white, red, and black), white phosphorus is generally excluded from the use as battery materials for its high reactivity and toxicity.[38] It has been reported that amorphous red phosphorus has a charge capacity of 897 mAh/g and discharge capacity of 15 mAh/g,[13] showing irreversible sodium insertion. Closely resembling graphite, black phosphorus has the most interesting structure among these allotropic forms, and is better suited as an electrode material. With a layered structure, black phosphorus is more stable and has a higher electrical conductivity than red phosphorus.[39] Within the same layer, each phosphorus atom covalently binds with three neighbors, while van der Waals interactions operate between the layers. The interlayer spacing of black phosphorus (5.4 Å) is much larger than that of graphite (3.4 Å), suggesting that sodium ions can intercalate into black phosphorus much more easily than into graphite.[40] Recent experimental studies have shown that black phosphorus exhibits a much higher charge (2035 mAh/g) and discharge (637 mAh/g) capacities than red phosphorus.[13] It has also been reported that a graphene–phosphorene hybrid yields even higher capacity and more stable cyclability.[38]

Electrochemical charging of black phosphorus involves a two-step sodiation process in series: intercalation followed by alloying.[38] Different from the flat layers in graphite, the layers in black phosphorus are puckered, with the pucker channels aligned along the [100] direction, as schematically shown in Figure 1. In the first step of sodiation (intercalation), sodium ions insert into black phosphorus along the pucker channels and fill out the interlayer space until a phase $Na_{0.25}P$ is formed.[38,40] The intercalation expands the interlayer spacing but preserves the layered structure of black phosphorus. In the second step of sodiation (alloying), further accumulated sodium breaks the P—P bonds, transforming the layered structure to amorphous sodium phosphide (Na_3P) in the fully sodiated stage.

Black phosphorus shows anisotropic swelling upon sodiation.[38] The atomic mechanisms for the anisotropic swelling have not been explored, but possibly stem from the two intrinsic anisotropic properties: sodium diffusional directionality in black phosphorus and sodiation induced strain anisotropy. First, inherent to its pucker-layered structure, black phosphorus exhibits a "selective diffusional behavior" during the first step of intercalation.[41] As reported, regardless of the contacting geometry between the sodium source and the black phosphorus, sodium atoms preferably diffuse along the [100] direction. This is due to the much lower sodium diffusion barriers in the [100] direction than in the [010] and [001] directions. To be specific, the diffusion barrier is 0.18 eV in the [100] direction, while at least 0.76 eV in the other two directions.[40] Structurally, the puckers function as fast diffusion channels. During the second step of sodiation, because the layered structure is gradually transformed into an amorphous compound as the sodium concentration increases, sodium diffusion becomes isotropic. Second, unlike the cubic crystalline structure of c-Si for which lithium insertion induces isotropic strain (known as the chemical strain),[29,42] the orthotropically layered structure of black phosphorus endows anisotropic chemical strain, with much larger expansion along the [001] direction than other directions. The chemical strain anisotropy resembles that in layered graphene upon lithiation, where the
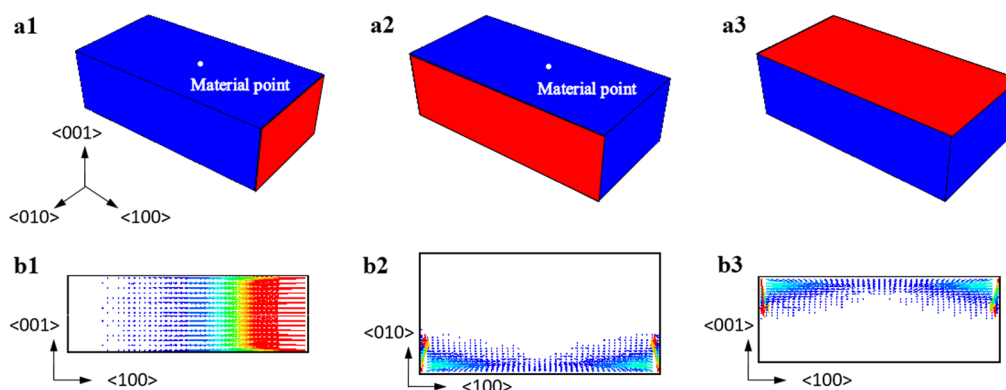
Figure 2. Sodiation starting from three different surfaces and the corresponding sodium flux patterns in the first step of sodiation. (a1−a3) Pristine crystalline black phosphorus blocks prior to sodiation, where the surfaces marked by red denote sodium sources. (b1−b3) Sodium fluxes in the first step of sodiation corresponding to different sodium sources in a1−a3, respectively. The material points indicate the location at which the stress evolution shown in Figure 5 is extracted.

expansion is predominant along the direction normal to the layers.[26,43−45]

A critical feature in lithiation of Si is the formation of sharp interphase that separates the Li-poor and Li-rich domains.[30,46,47] Though high-resolution transmission electron microscopy (TEM) imaging is yet to be conducted to resolve the atomic structure of the interphases, the nature of the interphases may be rationalized from the orientation and phase-dependent sodiation kinetics. Sodiation is a process involving chemical reaction and atomic diffusion in parallel. During sodiation, the tilted bonds of the puckers break first; further sodium accumulation and invasion breaks the bonds within the plane of the layer, followed by solid-state amorphization.[38,40] Because the first step of sodiation preserves the pucker-layered structure, the diffusivities remain nearly unchanged therefore leading to a diffuse interphase in all the directions. In the second step of sodiation, behind the reaction front sodium fast diffuses toward the interphase in an isotropic manner due to the amorphized structure and the consequently much reduced diffusional barriers in [010] and [001] directions. However, limited by the low diffusivity in the partially sodiated black phosphorus ($Na_{0.25}P$), the reaction front migrates very slowly along the [010] and [001] directions. This rate difference allows the Na-rich phase to easily catch up the reaction front and likely results in a sharp interphase along these two directions. However, along the [100] direction the comparable sodium diffusivity in front of and behind the reaction front renders a diffuse interphase. The diffuse interphase is also manifested by the gradual volume expansion along the [100] direction observed in experiments.[38] This two-step sodiation process of black phosphorus is in clear contrast to the two-step lithiation of amorphous Si (a-Si),[48−50] where a-Si is first lithiated to $Li_{2.5}Si$ by propagation of a sharp interphase and finally to $Li_{3.75}Si$ with an invisible diffuse interphase.

Our chemo-mechanical model incorporates the two-step sodiation and the 2-fold anisotropy, as well as the sharp and diffuse interphases. As the mechanical process is of a much shorter time scale, we assume that mechanical equilibrium is instantaneously met, while sodium transport is governed by the diffusion equation. In the first step of sodiation, sodium diffusivities are set to be orientation dependent with $D^1_{[100]} = 1000D^1_{[010]} = 1000D^1_{[001]}$ to capture the feature and avoid the numerical divergence. Here the superscript denotes the sodiation step, while the subscript denotes the orientation.

Note that the sodium diffusivities in [010] and [001] directions are set to be the same despite the different diffusional barriers because they are both negligibly small compared to that in the [100] direction. The diffusivities on the surfaces in the three directions are at least one order of magnitude larger than the ones in the same direction in the bulk, consistent with the much lower energy barriers for surface diffusion.[40,41] In the second step of sodiation, sodium diffusivities are set to be nonlinearly dependent on sodium concentration along the [010] and [001] directions: $D^2_{[010]} = D^2_{[001]} = D_0[1/(1 - c) - 2\alpha c]$,[42,51] where D_0 and α are tunable constants to control the interphase profile between the Na-rich and Na-poor phases and c is the sodium concentration. Along the [100] direction, the diffusivity remains unchanged from the first step. The cutoff value of the above nonlinear function is set to be $D^1_{cutoff} = D^1_{[100]} = D^2_{[100]}$ to ensure isotropic diffusion when c approaches unity. In our simulations, the two steps are distinguished by setting different Dirichlet boundary conditions. In the present model, the sodium concentration, c, is normalized by the fully sodiated phase of Na_3P, where $c = 1$ represents the Na_3P phase and $c = 0$ represents the pristine black phosphorus phase. Therefore, $c = 0.083$ is set to be the surface boundary condition for the first step of sodiation in order to match the composition of $Na_{0.25}P$, and $c = 1$ for the second step.

In the finite-strain framework, sodiation-induced deformation consists of the stretch rates and the spin rates. The total stretch rate is additive of the three components, the chemical ($\dot{\varepsilon}^c_{ij}$), elastic ($\dot{\varepsilon}^e_{ij}$), and plastic ($\dot{\varepsilon}^p_{ij}$), $\dot{\varepsilon}_{ij} = \dot{\varepsilon}^c_{ij} + \dot{\varepsilon}^e_{ij} + \dot{\varepsilon}^p_{ij}$.[42] The chemical stretch rate is assumed to be proportional to the increment of the sodium concentration, $\dot{\varepsilon}^c_{ij} = \beta_{ij}\dot{c}$. The diagonal tensor, β_{ij}, represents the sodiation expansion coefficients in three different directions, yielding chemical strain anisotropy. We set $\beta_{11} = 0$, $\beta_{22} = 0.92$, $\beta_{33} = 1.6$, and $\beta_{ij} = 0$ for the other entries, where β_{11}, β_{22}, and β_{33} are corresponding expansions in the [100], [010], and [001] directions, respectively. The elastic stretch rate, $\dot{\varepsilon}^e_{ij}$, obeys Hooke's law with the stiffness tensor, C_{ijkl}, of the orthotropic crystals. As the crystalline black phosphorus evolves into the amorphous sodium phosphide during sodiation, the material changes from orthotropic to isotropic.[52] Correspondingly, the stiffness tensor changes from nine independent materials constants for the unsodiated stage to only two for the fully sodiated stage (i.e., Young's modulus E and Poisson's ratio ν). For the intermediate states of charge, the stiffness tensor is assumed to be linearly dependent on sodium concentration,
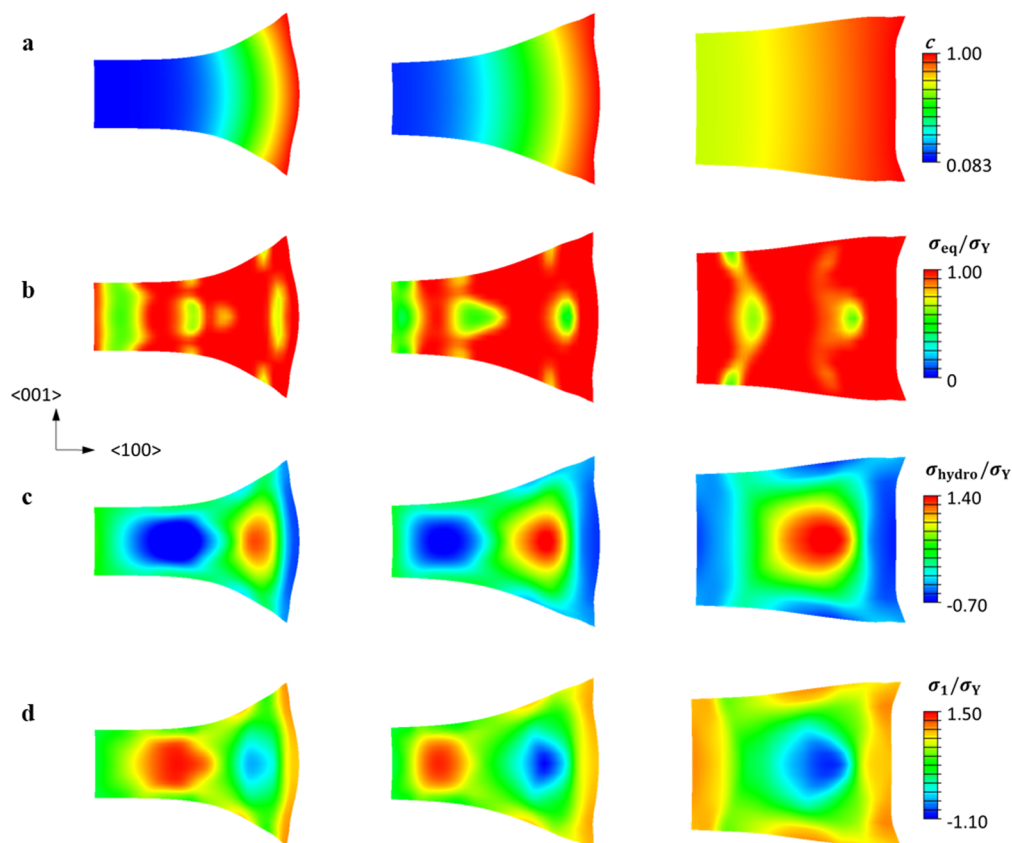
Figure 3. (a) Sodium concentration profile and (b) the equivalent stress, (c) the hydrostatic stress, and (d) the first principal stress distributions in the second step of sodiation with sodium source on the {100} surface.
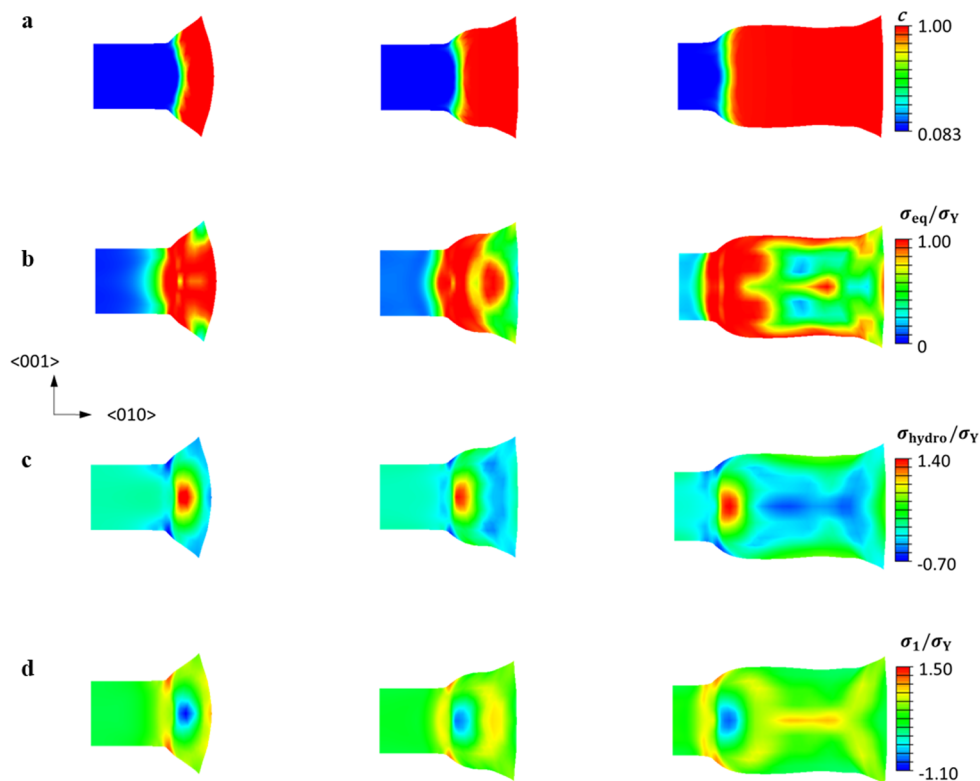
Figure 4. (a) Sodium concentration profile and (b) the equivalent stress, (c) the hydrostatic stress, and (d) the first principal stress distributions in the second step of sodiation with sodium source on the {010} surface.
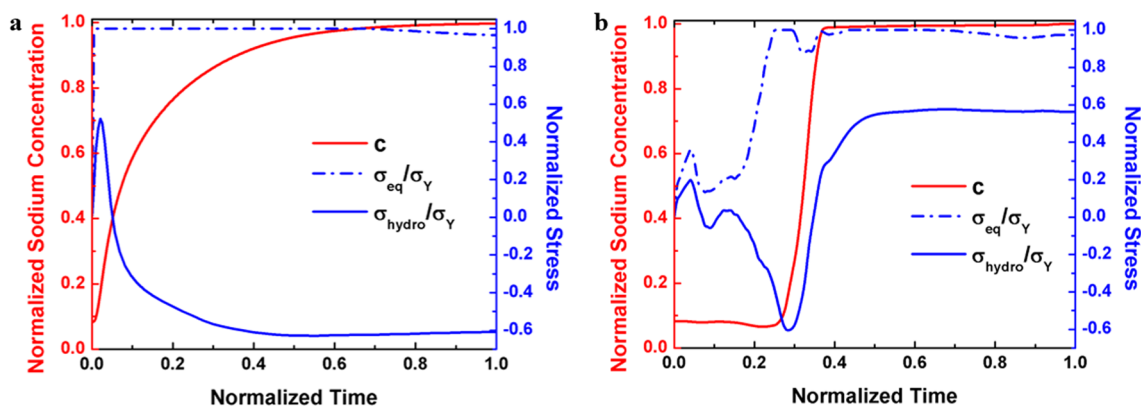
Figure 5. Evolution of equivalent stress (dash blue lines) and hydrostatic stress (solid blue lines) on a representative material point, along with the normalized sodium concentration (solid red lines). (a) Sodiation starts from {100} surface. (b) Sodiation starts from {010} surface.

interpolated by these two extreme states. The values of the elastic parameters used in our model are listed in the Supporting Information. The plastic stretch rate, $\dot{\varepsilon}_{ij}^{\mathrm{p}}$, obeys the classic J_2-flow rule. Namely, plastic yielding occurs when the equivalent stress, $\sigma_{\mathrm{eq}} = (3s_{ij}s_{ij}/2)^{1/2}$, reaches the yield stress, σ_Y = 1 GPa. Here $s_{ij} = \sigma_{ij} - \sigma_{kk}\delta_{ij}/3$ is the deviatoric part of Cauchy stress, σ_{ij}, and $\dot{\varepsilon}_{ij}^{\mathrm{p}}$ is proportional to s_{ij}. Note that we assume that both chemical and plastic deformations are spin-free.

We next apply the chemo-mechanical model to simulate sodiation of crystalline black phosphorus in a rectangular shape, as shown in Figure 2. Normalized by its length (along the [100] direction), its width (along the [010] direction) and height (along the [001] direction) are 0.5 and 0.35, respectively. Sodiation starts from one of the surfaces, colored in red (Figures 2a1−a3), by setting appropriate surface sodium concentration at relevant sodiation steps, as previously described. The back surface is set to be the symmetric plane. In the first step of sodiation, sodium fast fluxes from the {100} surface along the [100] direction (Figure 2b1). The flux patterns are markedly different from the cases when sodiation starts from the other two surfaces, {010} and {001}. As shown in Figure 2b2, when sodiated from the {010} surface, sodium first covers the end points of each pucker on the two {100} surfaces due to the higher diffusivity of the surface layers. Sodium atoms then enter the puckers from the two surfaces to the center by pucker-by-pucker diffusion along the [100] direction until the sodium concentration reaches 0.083 to form the Na$_{0.25}$P phase. The mechanism of sodiation from the {001} surface, shown in Figure 2b3, is similar to that from the {010} surface, except that the sodium now diffuses layer by layer, instead of pucker by pucker. Our simulations show that intercalation induced mechanical stress is comparatively small in the first step of sodiation (Figures S1 and S2). Therefore, in the next we only discuss stress generation in the second step.

Figures 3 and 4 plot the sodium concentration profiles at representative snapshots in the second step of sodiation and the corresponding mechanical stress, when sodiation starts from the {100} and {010} surfaces, respectively. Since sodium diffusion kinetics and stress generation are similar when sodiation starts from the {010} and {001} surfaces, we here only present one of the two cases. In Figure 3a, when sodiation starts from the {100} surface, a diffuse interphase forms along the [100] direction, whereas a sharp interphase develops along the [010] direction when starting from the {010} surface, as shown in Figure 4a. In Figure 4a, though the phosphorus near the sodium source surface is fully sodiated, the materials expand

to the extent much less than that set by β_{33} in the [001] direction. This deformation mode is due to the interplay between the diffusional anisotropy and chemical strain anisotropy. On the Na-rich side of the sharp interphase, the sodiated phosphorus undergoes ∼500% volume expansion. However, the partially sodiated black phosphorus (Na$_{0.25}$P) in front of the sharp interphase constrains the expansion. The volume expansion along with the sharp interphase generates large mismatch stress, resulting in large plastic flow near the interphase (Figure 4b). Because of the constraint of the partially sodiated black phosphorus to the plastic flow, the materials cannot expand freely in the [001] direction, but flow to the other directions to accommodate the volume expansion. In contrast, when sodiation starts from the {100} surface, although the material still plastically yields near the diffuse interphase (Figure 3b), the constraining effect of the diffuse interphase is much weaker. As a result, the expansion in three directions conforms to the chemical strain anisotropy set by β_{ij} (with a difference from the elastic deformation). The swelling phenomena manifest that these two anisotropic factors interact with one another. In particular, the anisotropic sodium diffusion generates sharp interphases along the [010] and [001] directions, which modify the intrinsic chemical strain anisotropy to shape the fully sodiated morphologies.

We next examine the evolution of the hydrostatic stress and the first principal stress during the second step of sodiation, normalized by the yield strength. Figures 3c and 4c plot the contours of the hydrostatic stress on the central plane perpendicular to the sodium source surfaces, corresponding to the charge mechanisms shown in Figures 3a and 4a, respectively. As a general feature for both cases, the cross sections near the interphase undergo compression (denoted by red color). The compressive region for sodiation from the {100} surface (Figure 3c) is markedly larger than that from the {010} surface (Figure 4c). This is likely due to the unloading effect behind the sharp interphase for the latter case (Figure 4b) as the sharp interphase sweeps forward. This unloading effect also leads to lower magnitude of the compression stress in the latter case (Figure 4c) than in the former one (Figure 3c). The distributions of the first principal stress for both cases are shown in Figures 3d and 4d. Interestingly, when sodiation starts from the {100} surface, the largest first principal stress occurs in the front of the diffuse interphase in the bulk. In contrast, when sodiation starts from the {010} surface, it appears on the surface at the sharp interphase. These indicate different failure modes; interior fracture occurs when sodiation
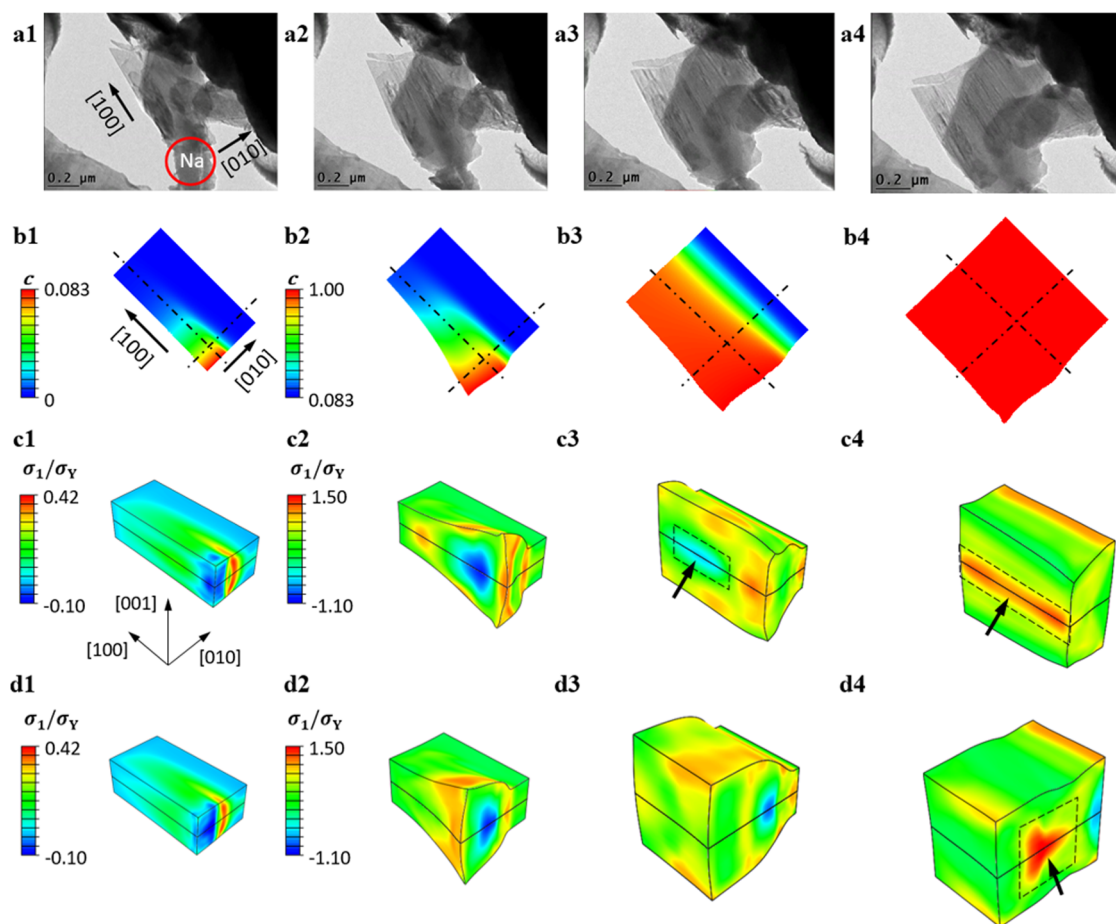
Figure 6. Comparisons between experiment and simulation results during the sodiation of black phosphorus. (a1−a4) TEM images showing the volumetric expansion of black phosphorus during sodiation.[38] (b1−b4) The sodium concentration profiles in the first step (b1) and in the second step (b2−b4) of sodiation, respectively. (c1−c4) The first principal stresses on the {010} cross-section the first (c1) and second step (c2−c4) of sodiation. (d1−d4) The first principal stresses on the {100} cross-section in the first (d1) and second (d2−d4) step of sodiation. The cross sections are indicated in (b1−b4) by the black dash lines. Regions of low stress due to the cancellation effect (c3) and of the largest first principal stresses at the fully sodiation stage (c4 and d4) are marked by dash boxes and pointed by arrows.

starts from the {100} surface, whereas surface fracture occurs when from the {010} surface.

To further illustrate the stress generation, we next plot the stress evolution of a representative material point, located at the center of the top surface, as shown in Figures 2a1,a2. Figure 5a,b presents the equivalent and hydrostatic stresses, along with the sodium concentration profiles, when sodiation starts from the {100} and {010} surfaces, respectively. The sodiation time is normalized by the corresponding time duration to fully sodiated the black phosphorus in the second step. As shown in Figure 5a, when the sodium concentration increases gradually along the [100] direction, the equivalent stress rises sharply to the yield strength. This indicates that the surface yields instantaneously at the beginning of the second step of sodiation due to the large volume expansion. The hydrostatic stress at the surface point is first in compression, then changes to tension, and finally reaches a maximum when the sodium concentration reaches ∼0.9. In Figure 5b, when sodiation starts from the {010} surface, the sharp interphase reaches the material point at $t = 0.25$ and sweeps through the point at $t = 0.4$. The material point yields even before the interphase arrives because of the large incompatible strain induced by the sharp interphase. It should be noted that the hydrostatic stress on the surface is compressive when the material is fully sodiated. The

compressive hydrostatic stress may be caused by severe plastic flow. As mentioned previously, because the expansion is constrained in the [001] direction, newly generated volume plastically flows to the [100] and [010] directions and subsequently resulting in the overall compressive hydrostatic stress on the surface. This result demonstrates that the diffusional anisotropy causes hydrostatic stress of opposite signs on the surface when sodiation starts from different crystal facets.

We further validate our model by a recent in situ TEM experiment on the sodiation of crystalline black phosphorus.[38] In the experiment, the phosphorus electrode underwent potentiostatic sodiation with a natively grown Na_2O layer on the sodium electrode as the solid electrolyte. The sodium electrode was then brought into contact with the black phosphorus to initiate sodiation (Figure 6a1). Consistent with the experimental settings, we set a small region on the {100} surface as the sodium source boundary condition in our model. The sodium concentration contour at a representative sodiation time in the first step of sodiation is plotted in Figure 6b1. The first principal stresses in the first step are much smaller than those in the second step (Figures 6c1,d1). At the initial stage of the second step, as shown in Figure 6b2, a diffuse interphase forms along the [100] direction, while a sharp

interphase along [010] direction. This sodiation mode can thus be regarded as a combination of the cases with sodium sources on both the {100} and {010} surfaces. Because sodiation proceeds much faster in the [100] direction than in the [010] direction, a sharp interphase parallel to the [100] direction is developed with nearly fully sodiated phase behind the interphase (Figure 6b3), which compares with the experiment observation shown in Figure 6a3. As indicated by the dash lines in Figure 6b2−b4, we depict the first principal stress profiles on the cross sections containing diffuse and sharp interphases in Figure 6c2−c4, d2−d4, respectively. The stress profiles share the similar general features as observed in the single-sodium-source cases, that is, high first principal stresses occur in the front of the diffuse interphase in the bulk and near the sharp interphase on the surface. However, the distribution of the first principal stress in Figure 6c3 is different from that of the single-directional case (Figure 3d) due to a cancellation effect. Specifically, because compression occurs inside the diffuse interphase (Figure 3d) and tension behind the sharp interphase (Figure 4d) in the single-surface-source sodiation cases, as discussed previously, these two stresses cancel out to certain extent, resulting in a relatively low stress state far from the sodium source behind the sharp interphase (Figure 6c3, pointed by the arrow). The largest first principal stress in this two-surface-source sodiation case appears at the fully sodiation stage in the bulk (c4 and d4, pointed by the arrows), indicating interior fracture. However, the nucleation site of fracture, indicated by the location with the highest tension, is different from the case when sodiation starts the {100} surface (Figure 3d). Our model further predicts that the expansions are 1.36%, 91.7%, and 153.6% along the [100], [010], and [001] directions, respectively, which are in good agreement with the experimentally measured data 0%, 92%, and 160%, respectively.[38]

We conclude that the apparent anisotropic swelling of sodiated black phosphorus is originated from the coupled effect of the two intrinsic anisotropies, that is, sodium diffusional directionality and chemical strain anisotropy. In particular, the sodium diffusional directionality in the layered structure generates sharp interphases along the [010] and [001] directions, which modify the chemical strain anisotropy to shape the fully sodiated morphology. Though not discussed here, the chemical strain anisotropy would reciprocally modulate stress generation, which in turn modifies the diffusional anisotropy, causing sodiation speedup or retardation, as seen in lithiation of Si and Ge.[53−56] The coupling effect renders substantial difference in the stress generation and degradation when sodiation starts from different crystal facets: interior fracture when sodiation starts from a {100} facet but surface fracture when from a {010} or {001} facet. When sodiation starts simultaneously from two different facets, the interaction between the diffuse and sharp interphases alter the stress landscape, and consequently modify the fracture mechanism and/or nucleation sites of fracture. The modeling framework developed here is widely applicable to the study of lithiation or sodiation of layered crystals. Our findings provide rational guidance to mitigate the degradation of black phosphorus as the promising anode for the next-generation NIBs with improved durability and cyclability.

■ ASSOCIATED CONTENT

Ⓢ Supporting Information

The Supporting Information is available free of charge on the ACS Publications website at DOI: 10.1021/acs.nano-lett.6b05033.

Additional material constants and stress distributions in the first step of sodiation (PDF)

■ AUTHOR INFORMATION

Corresponding Author
*E-mail: suz10@psu.edu.

ORCID ⓞ

Tianwu Chen: 0000-0002-3183-1507

Notes

The authors declare no competing financial interest.

■ REFERENCES

(1) Kim, S. W.; Seo, D. H.; Ma, X. H.; Ceder, G.; Kang, K. *Adv. Energy Mater.* **2012**, *2*, 710−721.
(2) Slater, M. D.; Kim, D.; Lee, E.; Johnson, C. S. *Adv. Funct. Mater.* **2013**, *23*, 947−958.
(3) Ellis, B. L.; Makahnouk, W. R. M.; Makimura, Y.; Toghill, K.; Nazar, L. F. *Nat. Mater.* **2007**, *6*, 749−753.
(4) Barpanda, P.; Oyama, G.; Nishimura, S.; Chung, S. C.; Yamada, A. *Nat. Commun.* **2014**, *5*, 4358.
(5) Komaba, S.; Murata, W.; Ishikawa, T.; Yabuuchi, N.; Ozeki, T.; Nakayama, T.; Ogata, A.; Gotoh, K.; Fujiwara, K. *Adv. Funct. Mater.* **2011**, *21*, 3859−3867.
(6) Cao, Y. L.; Xiao, L. F.; Sushko, M. L.; Wang, W.; Schwenzer, B.; Xiao, J.; Nie, Z. M.; Saraf, L. V.; Yang, Z. G.; Liu, J. *Nano Lett.* **2012**, *12*, 3783−3787.
(7) Ellis, L. D.; Wilkes, B. N.; Hatchard, T. D.; Obrovac, M. N. *J. Electrochem. Soc.* **2014**, *161*, A416−A421.
(8) Marino, C.; Debenedetti, A.; Fraisse, B.; Favier, F.; Monconduit, L. *Electrochem. Commun.* **2011**, *13*, 346−349.
(9) Stevens, D. A.; Dahn, J. R. *J. Electrochem. Soc.* **2000**, *147*, 1271−1273.
(10) Qian, J. F.; Chen, Y.; Wu, L.; Cao, Y. L.; Ai, X. P.; Yang, H. X. *Chem. Commun.* **2012**, *48*, 7070−7072.
(11) Wang, J. W.; Liu, X. H.; Mao, S. X.; Huang, J. Y. *Nano Lett.* **2012**, *12*, 5897−5902.
(12) Bommier, C.; Luo, W.; Gao, W. Y.; Greaney, A.; Ma, S. Q.; Ji, X. *Carbon* **2014**, *76*, 165−174.
(13) Qian, J. F.; Wu, X. Y.; Cao, Y. L.; Ai, X. P.; Yang, H. X. *Angew. Chem., Int. Ed.* **2013**, *52*, 4633−4636.
(14) Wu, H.; Chan, G.; Choi, J. W.; Ryu, I.; Yao, Y.; McDowell, M. T.; Lee, S. W.; Jackson, A.; Yang, Y.; Hu, L. B.; Cui, Y. *Nat. Nanotechnol.* **2012**, *7*, 310−315.
(15) Yi, R.; Dai, F.; Gordin, M. L.; Sohn, H.; Wang, D. H. *Adv. Energy Mater.* **2013**, *3*, 1507−1515.
(16) Jia, Z.; Li, T. *Extreme Mech. Lett.* **2016**, *8*, 273−282.
(17) Lee, S. W.; Nix, W. D.; Cui, Y. *Extreme Mech. Lett.* **2015**, *2*, 15−19.
(18) Ryu, I.; Choi, J. W.; Cui, Y.; Nix, W. D. *J. Mech. Phys. Solids* **2011**, *59*, 1717−1730.
(19) Lee, S. W.; McDowell, M. T.; Berla, L. A.; Nix, W. D.; Cui, Y. *Proc. Natl. Acad. Sci. U. S. A.* **2012**, *109*, 4080−4085.

(20) Berla, L. A.; Lee, S. W.; Ryu, I.; Cui, Y.; Nix, W. D. *J. Power Sources* **2014**, *258*, 253−259.

(21) Ryu, I.; Lee, S. W.; Gao, H.; Cui, Y.; Nix, W. D. *J. Power Sources* **2014**, *255*, 274−282.

(22) Huang, J. Y.; Zhong, L.; Wang, C. M.; Sullivan, J. P.; Xu, W.; Zhang, L. Q.; Mao, S. X.; Hudak, N. S.; Liu, X. H.; Subramanian, A.; Fan, H.; Qi, L.; Kushima, A.; Li, J. *Science* **2010**, *330*, 1515−1520.

(23) Liu, X. H.; Wang, J. W.; Liu, Y.; Zheng, H.; Kushima, A.; Huang, S.; Zhu, T.; Mao, S. X.; Li, J.; Zhang, S.; Lu, W.; Tour, J. M.; Huang, J. Y. *Carbon* **2012**, *50*, 3836−3844.

(24) Liang, W.; Hong, L.; Yang, H.; Fan, F.; Liu, Y.; Li, H.; Li, J.; Huang, J. Y.; Chen, L.-Q.; Zhu, T.; Zhang, S. *Nano Lett.* **2013**, *13*, 5212−5217.

(25) Liang, W.; Yang, H.; Fan, F.; Liu, Y.; Liu, X. H.; Huang, J. Y.; Zhu, T.; Zhang, S. *ACS Nano* **2013**, *7*, 3427−3433.

(26) Yang, H.; Huang, X.; Liang, W.; van Duin, A. C. T.; Raju, M.; Zhang, S. *Chem. Phys. Lett.* **2013**, *563*, 58−62.

(27) Zhao, K.; Pharr, M.; Cai, S.; Vlassak, J. J.; Suo, Z. *J. Am. Ceram. Soc.* **2011**, *94*, s226−s235.

(28) Zhao, K. J.; Tritsaris, G. A.; Pharr, M.; Wang, W. L.; Okeke, O.; Suo, Z. G.; Vlassak, J. J.; Kaxiras, E. *Nano Lett.* **2012**, *12*, 4397−4403.

(29) Yang, H.; Huang, S.; Huang, X.; Fan, F. F.; Liang, W. T.; Liu, X. H.; Chen, L. Q.; Huang, J. Y.; Li, J.; Zhu, T.; Zhang, S. L. *Nano Lett.* **2012**, *12*, 1953−1958.

(30) Liu, X. H.; Zheng, H.; Zhong, L.; Huan, S.; Karki, K.; Zhang, L. Q.; Liu, Y.; Kushima, A.; Liang, W. T.; Wang, J. W.; Cho, J. H.; Epstein, E.; Dayeh, S. A.; Picraux, S. T.; Zhu, T.; Li, J.; Sullivan, J. P.; Cumings, J.; Wang, C. S.; Mao, S. X.; Ye, Z. Z.; Zhang, S. L.; Huang, J. Y. *Nano Lett.* **2011**, *11*, 3312−3318.

(31) Luo, L. L.; Yang, H.; Yan, P. F.; Travis, J. J.; Lee, Y.; Liu, N.; Piper, D. M.; Lee, S. H.; Zhao, P.; George, S. M.; Zhang, J. G.; Cui, Y.; Zhang, S. L.; Ban, C. M.; Wang, C. M. *ACS Nano* **2015**, *9*, 5559−5566.

(32) Luo, L. L.; Zhao, P.; Yang, H.; Liu, B. R.; Zhang, J. G.; Cui, Y.; Yu, G. H.; Zhang, S. L.; Wang, C. M. *Nano Lett.* **2015**, *15*, 7016−7022.

(33) Xiao, Q. F.; Gu, M.; Yang, H.; Li, B.; Zhang, C. M.; Liu, Y.; Liu, F.; Dai, F.; Yang, L.; Liu, Z. Y.; Xiao, X. C.; Liu, G.; Zhao, P.; Zhang, S. L.; Wang, C. M.; Lu, Y. F.; Cai, M. *Nat. Commun.* **2015**, *6*, 8844.

(34) Chan, C. K.; Peng, H.; Liu, G.; McIlwrath, K.; Zhang, X. F.; Huggins, R. A.; Cui, Y. *Nat. Nanotechnol.* **2008**, *3*, 31−35.

(35) Liu, N.; Wu, H.; McDowell, M. T.; Yao, Y.; Wang, C. M.; Cui, Y. *Nano Lett.* **2012**, *12*, 3315−3321.

(36) Wang, C.; Wu, H.; Chen, Z.; McDowell, M. T.; Cui, Y.; Bao, Z. A. *Nat. Chem.* **2013**, *5*, 1042−1048.

(37) Kim, S.; Choi, S. J.; Zhao, K.; Yang, H.; Gobbi, G.; Zhang, S.; Li, J. *Nat. Commun.* **2016**, *7*, 10146.

(38) Sun, J.; Lee, H. W.; Pasta, M.; Yuan, H. T.; Zheng, G. Y.; Sun, Y. M.; Li, Y. Z.; Cui, Y. *Nat. Nanotechnol.* **2015**, *10*, 980−U184.

(39) Morita, A. *Appl. Phys. A: Solids Surf.* **1986**, *39*, 227−242.

(40) Hembram, K. P. S. S.; Jung, H.; Yeo, B. C.; Pai, S. J.; Kim, S.; Lee, K. R.; Han, S. S. *J. Phys. Chem. C* **2015**, *119*, 15041−15046.

(41) Nie, A. M.; Cheng, Y. C.; Ning, S. C.; Foroozan, T.; Yasaei, P.; Li, W.; Song, B. A.; Yuan, Y. F.; Chen, L.; Salehi-Khojin, A.; Mashayek, F.; Shahbazian-Yassar, R. *Nano Lett.* **2016**, *16*, 2240−2247.

(42) Yang, H.; Fan, F. F.; Liang, W. T.; Guo, X.; Zhu, T.; Zhang, S. L. *J. Mech. Phys. Solids* **2014**, *70*, 349−361.

(43) Liu, Y.; Zheng, H.; Liu, X. H.; Huang, S.; Zhu, T.; Wang, J.; Kushima, A.; Hudak, N. S.; Huang, X.; Zhang, S.; Mao, S. X.; Qian, X.; Li, J.; Huang, J. Y. *ACS Nano* **2011**, *5*, 7245−7253.

(44) Huang, X.; Yang, H.; van Duin, A. C. T.; Hsia, K. J.; Zhang, S. *Phys. Rev. B: Condens. Matter Mater. Phys.* **2012**, *85*, 195453.

(45) Huang, X.; Yang, H.; Liang, W.; Raju, M.; Terrones, M.; Crespi, V. H.; van Duin, A. C. T.; Zhang, S. *Appl. Phys. Lett.* **2013**, *103*, 153901−4.

(46) Chon, M. J.; Sethuraman, V. A.; McCormick, A.; Srinivasan, V.; Guduru, P. R. *Phys. Rev. Lett.* **2011**, *107*, 045503.

(47) Liu, X. H.; Zhang, L. Q.; Zhong, L.; Liu, Y.; Zheng, H.; Wang, J. W.; Cho, J. H.; Dayeh, S. A.; Picraux, S. T.; Sullivan, J. P.; Mao, S. X.; Ye, Z. Z.; Huang, J. Y. *Nano Lett.* **2011**, *11*, 2251−2258.

(48) Wang, J. W.; He, Y.; Fan, F. F.; Liu, X. H.; Xia, S. M.; Liu, Y.; Harris, C. T.; Li, H.; Huang, J. Y.; Mao, S. X.; Zhu, T. *Nano Lett.* **2013**, *13*, 709−715.

(49) McDowell, M. T.; Lee, S. W.; Harris, J. T.; Korgel, B. A.; Wang, C. M.; Nix, W. D.; Cui, Y. *Nano Lett.* **2013**, *13*, 758−764.

(50) Jia, Z.; Li, T. *J. Mech. Phys. Solids* **2016**, *91*, 278−290.

(51) Huang, S.; Fan, F.; Li, J.; Zhang, S.; Zhu, T. *Acta Mater.* **2013**, *61*, 4354−4364.

(52) Appalakondaiah, S.; Vaitheeswaran, G.; Lebegue, S.; Christensen, N. E.; Svane, A. *Phys. Rev. B: Condens. Matter Mater. Phys.* **2012**, *86*, 035105.

(53) Gu, M.; Yang, H.; Perea, D. E.; Zhang, J. G.; Zhang, S. L.; Wang, C. M. *Nano Lett.* **2014**, *14*, 4622−4627.

(54) Yang, H.; Liang, W.; Guo, X.; Wang, C.-M.; Zhang, S. *Extreme Mech. Lett.* **2015**, *2*, 1−6.

(55) McDowell, M. T.; Ryu, I.; Lee, S. W.; Wang, C.; Nix, W. D.; Cui, Y. *Adv. Mater.* **2012**, *24*, 6034−6041.

(56) Liu, X. H.; Fan, F.; Yang, H.; Zhang, S.; Huang, J. Y.; Zhu, T. *ACS Nano* **2013**, *7*, 1495−1503.